

Chapter 2

Ultra-low loss silicon nitride platform

This chapter introduces the ultra-low-loss silicon nitride platform which forms the basis of this work. The design considerations for the choice of waveguide geometry are discussed. Subsequently, models and practical considerations for the design of efficient directional couplers are also presented.

2.1 Silicon nitride waveguide design

Waveguides of silicon nitride core and silicon dioxide cladding have become an important technology for creating ultra-low-loss waveguides. Mode profiles of a few selected geometries are shown in Figure 2.1. Using standard CMOS processes, these waveguides may be fabricated at the wafer scale on silicon substrates as large as 300 mm in diameter [1, 2, 3, 4]. Thanks to the high quality of silicon dioxide and silicon nitride available using CMOS processes, the propagation loss is generally dominated by scattering losses, rather than material absorption. The primary component of scattering loss is generally sidewall

roughness of the silicon nitride core, as the top-surface and bottom-surface roughness of the silicon nitride layer are generally well below 1 nm owing to high quality CMP processes and conformal deposition techniques [5, 6]. By contrast, roughness – originating from the line-edge roughness of the lithography process – is transferred to the waveguide sidewall by the dry-etching process, and is generally over 1 nm in magnitude [7, 8]. This sidewall roughness amounts to a perturbation to the waveguide geometry as light propagates along the waveguide, resulting in light being scattered into the continuum of unguided modes [9], with scattering loss magnitude which is ultimately determined by the overlap between the guided optical mode and the waveguide sidewall. The choice of the thickness of the silicon nitride layer is thus critical, as it determines the degree to which the optical mode is influenced by sidewall roughness. Accordingly, several types of silicon nitride waveguides have emerged to serve various purposes.

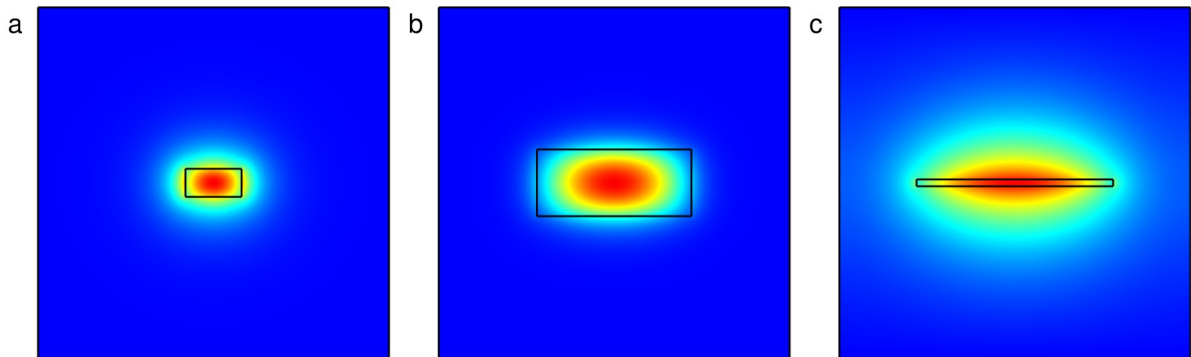


Figure 2.1: **Transverse-electric (TE) cross-sectional mode profiles** of silicon nitride waveguides featuring (a) 400 nm thickness and 800 nm width, (b) 950 nm thickness and 2200 nm width, and (c) 100nm thickness at 2800 nm width.

High-modal-confinement waveguides with thickness of up to 400 nm (shown in Figure 2.1a) have become commonplace in many commercial silicon photonics foundries. These waveguides feature a single transverse electric (TE) mode, a single transverse magnetic (TM) mode, bending radii as low as 20 μm , and propagation losses as low as 20 dB/m. They are frequently used for low-loss routing, or for coupling to fiber at the

edge of a PIC.

For applications in nonlinear optics, there is often a requirement that the waveguide exhibit anomalous group velocity dispersion, such as for bright soliton formation or supercontinuum generation via the Kerr effect [10, 11]. Anomalous dispersion requires a much larger waveguide thickness, generally above 700 nm (Figure 2.1b). These waveguides feature propagation losses as low as 1 dB/m [4, 5], as the optical mode within the larger core exhibits a lower overlap with the waveguide sidewall, as compared to the waveguide shown in Figure 2.1a. However, these waveguides support higher-order transverse modes. While bending radii as low as 20 μm are possible in this waveguide core geometry as well, care must be taken in routing between straight and bending waveguides to minimize modal cross-talk [12].

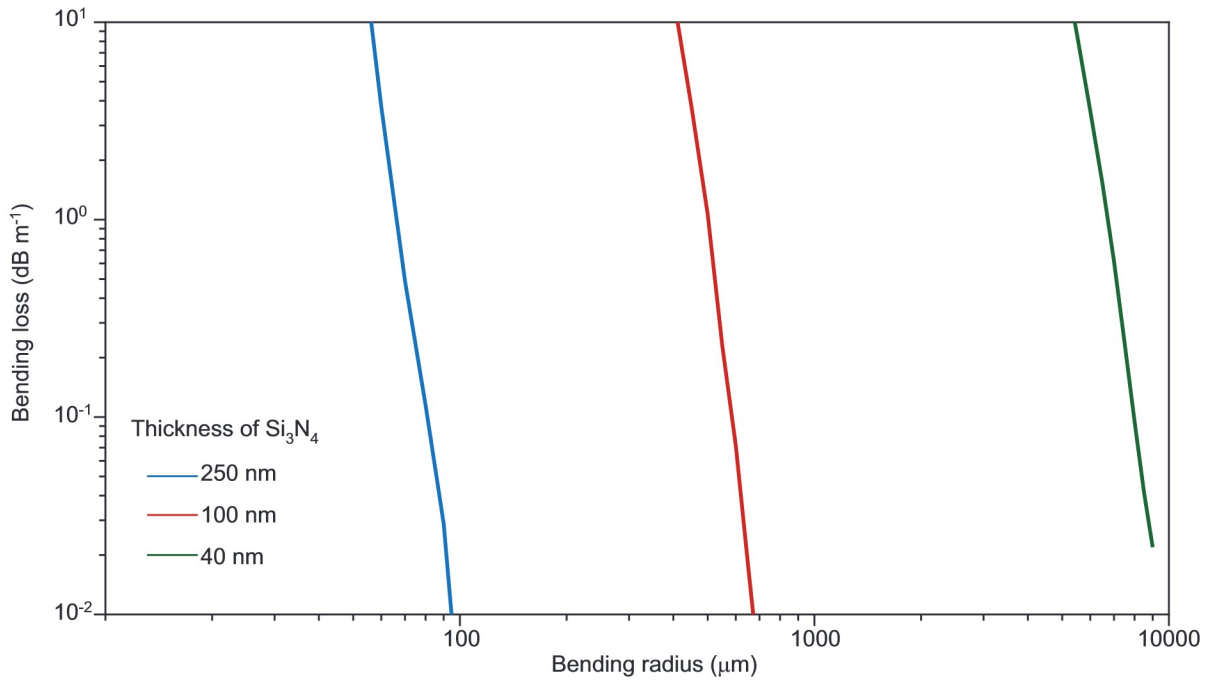


Figure 2.2: **Simulated bending loss** for the fundamental TE mode at $\lambda = 1550 \text{ nm}$ for silicon nitride waveguides of 250 nm, 100 nm, and 40 nm thickness, and 1.4 μm , 2.8 μm , and 5.6 μm width, respectively. The waveguide widths are chosen to support single-mode propagation within the telecommunications C-band. Reproduced from [13].

For applications seeking even lower waveguide loss, the thickness of the silicon nitride layer is a compromise between loss and the acceptable device footprint. Silicon nitride waveguides of thickness 100 nm or below (Figure 2.1c) form high-aspect ratio, low-confinement silicon nitride waveguides with propagation loss potentially below 0.1 dB/m [8, 7]. In this regime, the optical mode resides primarily within the silicon dioxide cladding. For decreasing silicon nitride thickness, the optical mode is increasingly 'squeezed out' of the core, and the mode volume grows [7] while the sidewall height shrinks. As a result, the sidewall overlap with the optical mode decreases, and the sidewall scattering loss is also reduced. However, as the optical mode grows, the minimum feasible bend radius also grows. The dependence of bending loss on bending radius for single-mode waveguide geometries at a selected silicon nitride thickness is shown in Figure 2.2, demonstrating that the selection of thinner waveguide cores to achieve a lower propagation loss comes at the expense of increasing bending radius and thus device footprint. Indeed, a core thickness of 40 nm necessitates a minimum bending radius approaching 1 cm, such that a standard deep-UV lithography reticle of approximately 2 cm by 2 cm dimension may hardly accommodate a single device. For the remainder of this chapter, we will consider silicon nitride waveguides with approximately 100 nm thickness, which enable extremely low propagation loss and bending radius below 1 mm.

A cross-sectional diagram of the waveguide geometry considered is shown in Figure 2.3. The waveguide fabrication follows the general process as detailed in [7, 13]. First, a silicon dioxide layer is formed by thermal oxidation of a silicon wafer with thickness 14.5 μm . A 100 nm layer of silicon nitride is deposited via low-pressure chemical vapor deposition (LPCVD), patterned using deep UV (DUV) stepper lithography, and dry-etched to form the waveguide core. Then, LPCVD silicon dioxide is deposited from a tetra-ethyl ortho-silicate (TEOS) precursor and annealed at 1150 °C to reach a total top cladding thickness of 2 μm and a total annealing time exceeding 20 hours.

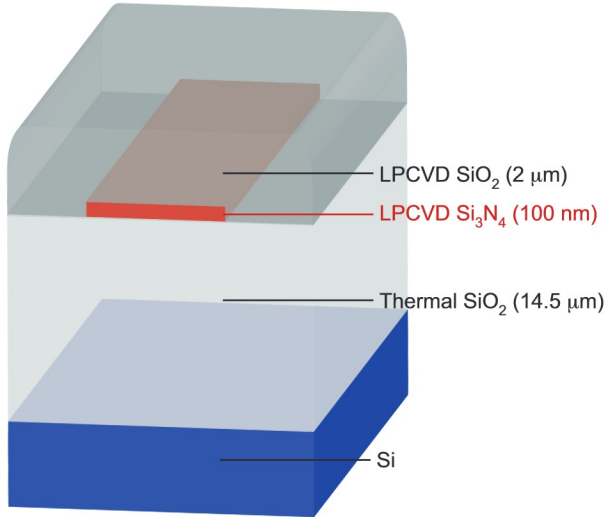


Figure 2.3: **Cross-sectional diagram of the ultra-low-loss waveguide** consisting of silicon nitride as the core material, silica as the cladding and silicon as the substrate (not to scale). Reproduced from [13].

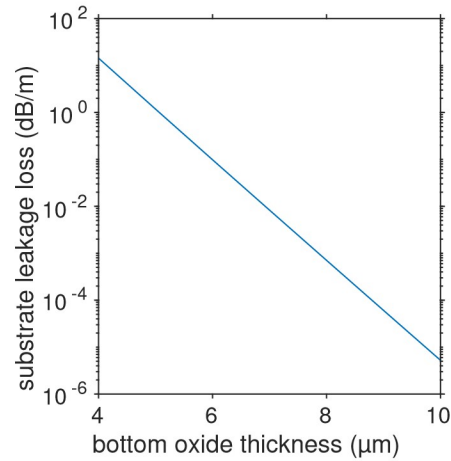


Figure 2.4: **Loss due to radiation into the silicon substrate** as a function of bottom silicon dioxide cladding thickness for a 100 nm thick, 2800 nm wide silicon nitride waveguide with 2 μm top cladding, simulated at 1550 nm wavelength.

The choice of lower cladding thickness is constrained by leakage into the silicon substrate. The dependence of substrate leakage on lower silicon dioxide cladding thickness is shown in Figure 2.4 for a 100 nm thick silicon waveguide at single-mode width of 2800 nm. A lower cladding thickness of 8 μm or greater is sufficient to guarantee a substrate leakage below 0.001 dB/m in this geometry. We select 14.5 μm lower cladding thickness to ensure negligible substrate leakage for a wide range of silicon nitride thickness and waveguide width, and over a wide range of operating wavelengths.

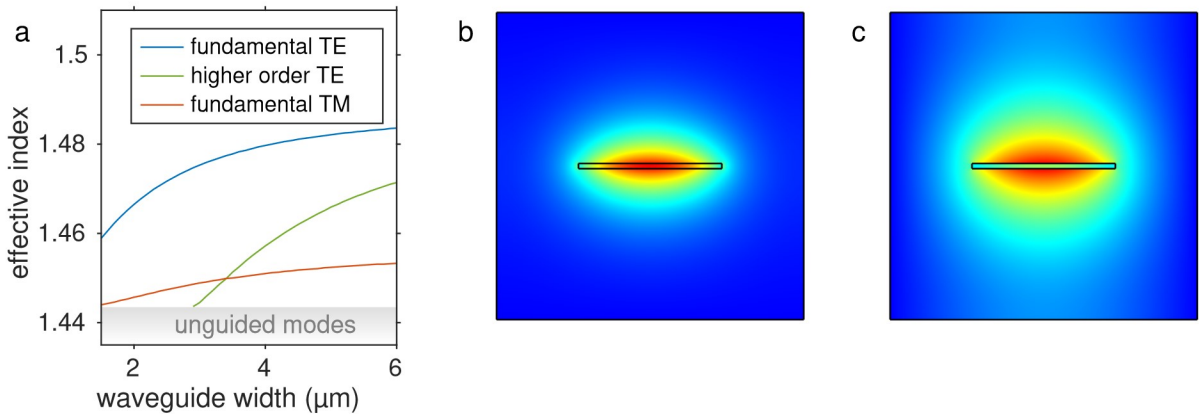


Figure 2.5: Single mode condition. (a) Plot of modal index as a function of waveguide width for a 100 nm thick silicon nitride waveguide, simulated at 1550 nm. Below 3 μm waveguide width, only a single TE-polarized mode, and a single TM-polarized mode are supported. The continuum of unguided optical modes within the silicon dioxide cladding are indicated by the shaded region. (b) Electric field magnitude for the fundamental TE mode at 2.8 μm width. (c) Electric field magnitude for the fundamental TM mode at 2.8 μm width.

For a given core material thickness, the single-mode condition can be determined by simulating the effective indices of the guided modes over a range of waveguide widths. Such a study is shown in Figure 2.5a, demonstrating that the higher-order TE-polarized mode is cut off for width below 3 μm . A choice of 2.8 μm width ensures that the waveguide remains single mode over a wide range of operating wavelength, as well as thickness deviations (to account for fabrication process tolerances). The modal profiles of the guided TE and TM modes at this width are shown if Figure 2.5b,c. However, while both

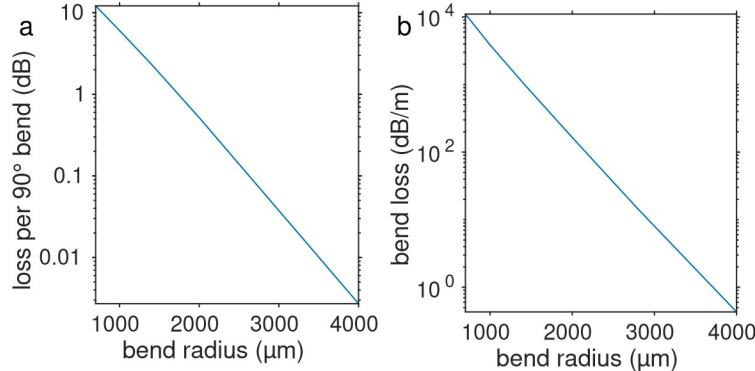


Figure 2.6: **Bending loss modeling.** (a) loss per bend and (b) loss per meter, of the fundamental TM mode for a 100 nm thick, 2.8 μm wide waveguide as a function of bend radius at 1550 nm wavelength.

TE and TM polarizations may be guided in a straight waveguide, the bending waveguide exhibits significant polarization-dependent loss, as shown in Figure 2.6. For bending below 1 mm, the bending loss of the TM mode approaches 10 dB per 90° bend, and may be used as an on-chip polarizer [14]. Due to the high propagation loss of the fundamental TM mode around bends, a waveguide featuring 2.8 μm width and bends at 1 mm bend radius or below may be considered to support only a single mode.

2.2 Resonator modeling

Optical resonators confine light to small volumes by resonant recirculation. Low optical losses provide a dual benefit to these devices. First, by dramatically enhancing light intensity within the resonator, low losses make it possible to access nonlinear effects. Secondly, low losses enable to resonators to exhibit narrow resonant bandwidths, enabling high-quality optical filters [15]. These properties of resonators make them a fundamental building block in many optical systems.

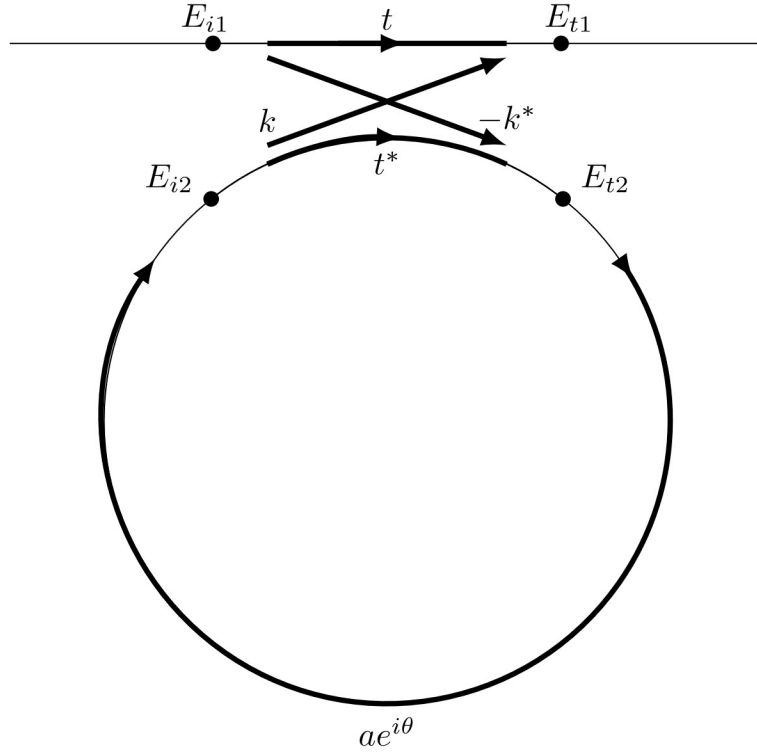


Figure 2.7: **Generic representation of a ring resonator** coupled to a single waveguide, based on [16, 17, 18].

2.2.1 Block element model

A simple way to form a resonator is to route a waveguide in a closed loop, allowing the light to recirculate. In order to excite the resonator, another waveguide, known as the bus waveguide, is brought into close spatial proximity, allowing light to couple across the gap. This basic configuration is depicted in Figure 2.7, and is based on the model presented in [16, 17, 18]. This system can be modeled by a linear system of equations in terms of the complex electric fields within the resonator and bus waveguides. The coupling region may be described by the matrix equation [16]

$$\begin{pmatrix} E_{t1} \\ E_{t2} \end{pmatrix} = \begin{pmatrix} t & k \\ -k^* & t^* \end{pmatrix} \begin{pmatrix} E_{i1} \\ E_{i2} \end{pmatrix} \quad (2.1)$$

Assuming that the coupler is lossless, the coupling matrix is unitary, and the coupling coefficients through and across the coupling region may be written in terms of one another.

$$|k^2| + |t^2| = 1 \quad (2.2)$$

Finally, the self-coupling of the resonator may be described by the following equation, where the phase accumulated propagating around the resonator waveguide is represented by θ , and the attenuation of the resonator waveguide per round-trip is represented by a .

$$E_{i2} = a \cdot e^{i\theta} E_{t2} \quad (2.3)$$

By normalizing the input field, $E_{i1} = 1$, then the system of equations may be solved for the field within the resonator, as well as the output power [18].

$$E_{t2} = \frac{-k^*}{1 - at^*e^{i\theta}} \quad (2.4)$$

$$P_{t1} = |E_{t1}|^2 = \frac{a^2 + |t|^2 - 2a|t|\cos(\theta)}{1 + a^2|t|^2 - 2a|t|\cos(\theta)} \quad (2.5)$$

The coupler region and waveguides may also be expressed as transmission matrices and solved by the transmission matrix method [19], which allows for modeling larger structures, including resonators with two bus waveguides, as well as multi-ring structures.

2.2.2 Rate equation model

Ring resonators may equivalently be described by a simple oscillator model [20]. In this model, A represents the time-varying, complex, electric field within the resonator, S represents the time-varying electric field at the input of the bus waveguide, T is the

transmitted electric field, ω_0 represents the resonance frequency, τ represents the photon lifetime within the resonator, k represents the amount of light coupled through the waveguide coupler in a single pass, and κ represents the coupling rate of the electric field through the coupler.

$$\frac{d}{dt}A = \left(i\omega_0 - \frac{1}{2\tau}\right)A + \kappa S \quad (2.6)$$

$$T = -S + kA \quad (2.7)$$

This first-order differential equation may be solved for A , yielding the standard equation for a Lorentzian resonance shape (Equation 2.8).

$$A = \frac{\kappa S}{i(\omega - \omega_0) + \frac{1}{2\tau}} \quad (2.8)$$

Notably, Equation 2.4 may also be written in this form by first-order Taylor expansion of the exponential term in the denominator. The physical parameters described in the previous section may be related to the oscillator model parameters as follows.

$$\kappa = k \frac{c}{n_g L} \quad (2.9)$$

L represents the round-trip length of the resonator; n_g represents the group index of the waveguide.

$$1/\tau = 1/\tau_0 + 1/\tau_{ex} \quad (2.10)$$

As τ represents the effective lifetime of the cavity as a whole, it is comprised of both the intrinsic photon lifetime, τ_0 , as well as the coupler lifetime, τ_{ex} . As in the prior section, k denotes the light transferred by the coupler from the bus waveguide to the resonator in a single pass, and a denotes the electric field attenuation per round trip of

the resonator.

$$1/\tau_{ex} = k^2 \frac{c}{n_g L} \quad (2.11)$$

$$1/\tau_0 = (1 - a^2) \frac{c}{n_g L} \quad (2.12)$$

In ultra-high Q factor microresonators, Rayleigh backscattering within the resonator can lead the splitting of a single resonance into a doublet, due to mutual coupling of the forward and backward propagating electric fields. The oscillator model can be expanded to include backscattering as well by including a coupling rate between forward and backward modes [20].

$$\frac{d}{dt} \begin{pmatrix} A_{\text{cw}} \\ A_{\text{ccw}} \end{pmatrix} = \begin{pmatrix} i\omega_0 - \frac{1}{2\tau} & i\beta \\ i\beta & i\omega_0 - \frac{1}{2\tau} \end{pmatrix} \begin{pmatrix} A_{\text{cw}} \\ A_{\text{ccw}} \end{pmatrix} + \kappa \begin{pmatrix} S \\ 0 \end{pmatrix} \quad (2.13)$$

A_{cw} represents the forward, clockwise propagating field, A_{ccw} represents the backwards, counter clockwise propagating field, and β is the backscattering-induced coupling rate between the two fields. If the backscattering coefficient per unit length, b , of the waveguide (generally expressed in units of dB/mm) is known [21], then the two may be related as follows

$$\beta = \sqrt{bL} \frac{c}{n_g L} \quad (2.14)$$

This model is used later in the chapter to model the measured transmission spectra of ultra-high Q resonators exhibiting doublet lineshapes.

2.3 Directional coupler design

2.3.1 Coupled mode theory

The operation of the coupling region discussed in the optical resonator models of the previous sections, and shown in Figure 2.7, can be described using either a two-state coupled mode theory [19] or two-state time-dependent perturbation theory [22], which are equivalent but for the choice of dependent variable: space, in the case of coupled mode theory; time, in the case of time-dependent perturbation theory. For a more complete treatment, refer to [22, 19, 23]. The necessary conclusions are summarized as follows.

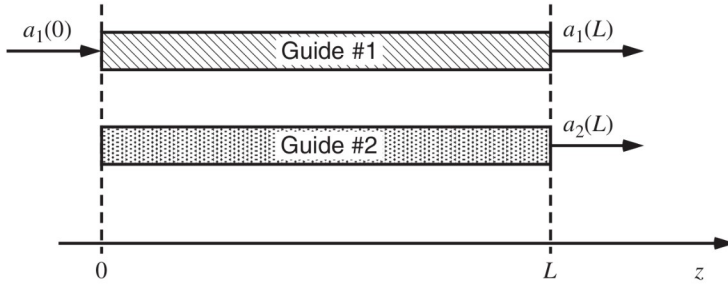


Figure 2.8: **Generic representation of a four-port directional coupler**, reproduced from [19].

A generic four-port directional coupler is shown in Figure 2.8. It is noted that while the figure implies propagation along the z -axis of a Cartesian coordinate system, the following equations work equally well along the azimuth direction of a cylindrical coordinate system, θ , (a concentric directional coupler), and the following equations may be adapted to a cylindrical coordinate system by simply replacing z with θ . The electric field at the position z within two parallel waveguides are described by $a_1(z)$ and $a_2(z)$, respectively. The evolution of the fields within the directional coupler are governed by

the following differential equation.

$$i \frac{d}{dz} \begin{pmatrix} a_1(z) \\ a_2(z) \end{pmatrix} = \begin{pmatrix} \beta_{11} & \beta_{12} \\ \beta_{21} & \beta_{22} \end{pmatrix} \begin{pmatrix} a_1(z) \\ a_2(z) \end{pmatrix} \quad (2.15)$$

β_{11} represents the propagation constant of the mode propagating in the first waveguide, and β_{22} represents the propagation constant of the mode propagating in the second waveguide. β_{12} and β_{21} represent the coupling strength between the two modes and are generally equal to one another. The differential equation may be solved by making the following substitution.

$$a_n(z) = c_n(z)e^{-i\beta_{nn}z} \quad (2.16)$$

After substitution, the differential equation may be written as follows.

$$i \frac{d}{dz} \begin{pmatrix} c_1(z) \\ c_2(z) \end{pmatrix} = \begin{pmatrix} 0 & \beta_{12}e^{-i\delta\beta z} \\ \beta_{21}e^{i\delta\beta z} & 0 \end{pmatrix} \begin{pmatrix} c_1(z) \\ c_2(z) \end{pmatrix} \quad (2.17)$$

The propagation constant mismatch, $\delta\beta$, between the two waveguides is defined as follows.

$$\delta\beta = \beta_{22} - \beta_{11} \quad (2.18)$$

For the initial condition $a_1(0) = 1$, $a_2(0) = 0$, the differential equation may then be solved to obtain a closed-form solution for the evolution of the electric fields within the directional coupler.

$$c_1(z) = \left(\cos Bz + \frac{i\delta\beta}{2B} \sin Bz \right) e^{-i\delta\beta z/2} \quad (2.19)$$

$$c_2(z) = -\frac{i\beta_{21}}{2B} \sin(Bz)e^{+i\delta\beta z/2} \quad (2.20)$$

Where the oscillation frequency describing the transfer of power between the modes, B is given by the following equation.

$$B^2 = |\beta_{21}|^2 + \left(\frac{\delta\beta}{2}\right)^2 \quad (2.21)$$

The total power coupled across the directional coupler, as a function of directional coupler length, is then given by $|c_2(z)|^2$.

$$|c_2(z)|^2 = C^2 \sin^2 Bz \quad (2.22)$$

Where the maximum amount of power transferred between the waveguides is given by the following equation

$$C^2 = \frac{|\beta_{21}|^2}{(\frac{1}{2}\delta\beta)^2 + |\beta_{21}|^2} \quad (2.23)$$

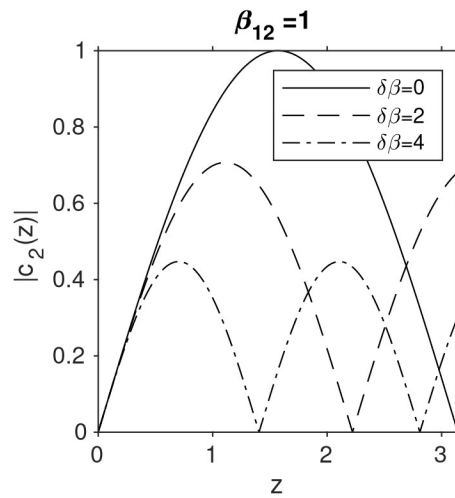


Figure 2.9: Influence of coupling rate and mismatch on coupling coefficient.
Coupled field amplitude across a directional coupler for various values of propagation constant mismatch, at a fixed coupling rate $\beta_{12} = 1$.

This equation suggests an oscillatory transfer of power between the two waveguides, which is identical to the phenomenon of Rabi oscillations in quantum mechanics. The dependence of coupled electric field on coupler length for a selection of propagation constant mismatch is shown in Figure 2.9.

2.3.2 Calculation of the inter-modal coupling rate

The calculation of β_{21} may be carried out in two ways. It can be calculated from the mode overlap integral [19].

$$\beta_{12} = \frac{k_0^2}{2\beta_1} \frac{\int (\epsilon_1 - \epsilon_c) \mathbf{U}_1^* \cdot \mathbf{U}_2 dA}{\int |U_1|^2 dA} \quad (2.24)$$

$$\beta_{21} = \frac{k_0^2}{2\beta_2} \frac{\int (\epsilon_2 - \epsilon_c) \mathbf{U}_2^* \cdot \mathbf{U}_1 dA}{\int |U_2|^2 dA} \quad (2.25)$$

Where $\mathbf{U}_{1,2}$ are the normalized electric field distribution of the modes of the individual waveguides, $\epsilon_{1,2}$ are the dielectric constant profiles of each individual waveguide, and ϵ_c is the dielectric constant profile in the absence of both waveguides, and k_0 is the free-space wavenumber. However, the equation 2.21 suggests a straightforward method to infer the coupling rate without calculating an overlap integral. Simulation of the eigenmodes of the directional coupler will result in the coupled super-modes, which are superpositions of the modes of the individual waveguides. If the super-modes of the system have propagation constants β_x and β_y , then their difference represents the Rabi oscillation frequency

$$B = \frac{\beta_x - \beta_y}{2} \quad (2.26)$$

The propagation constant mismatch, $\delta\beta$, can be calculated from the propagation constants of the isolated waveguides (Equation 2.18), which can in turn be used to calculate

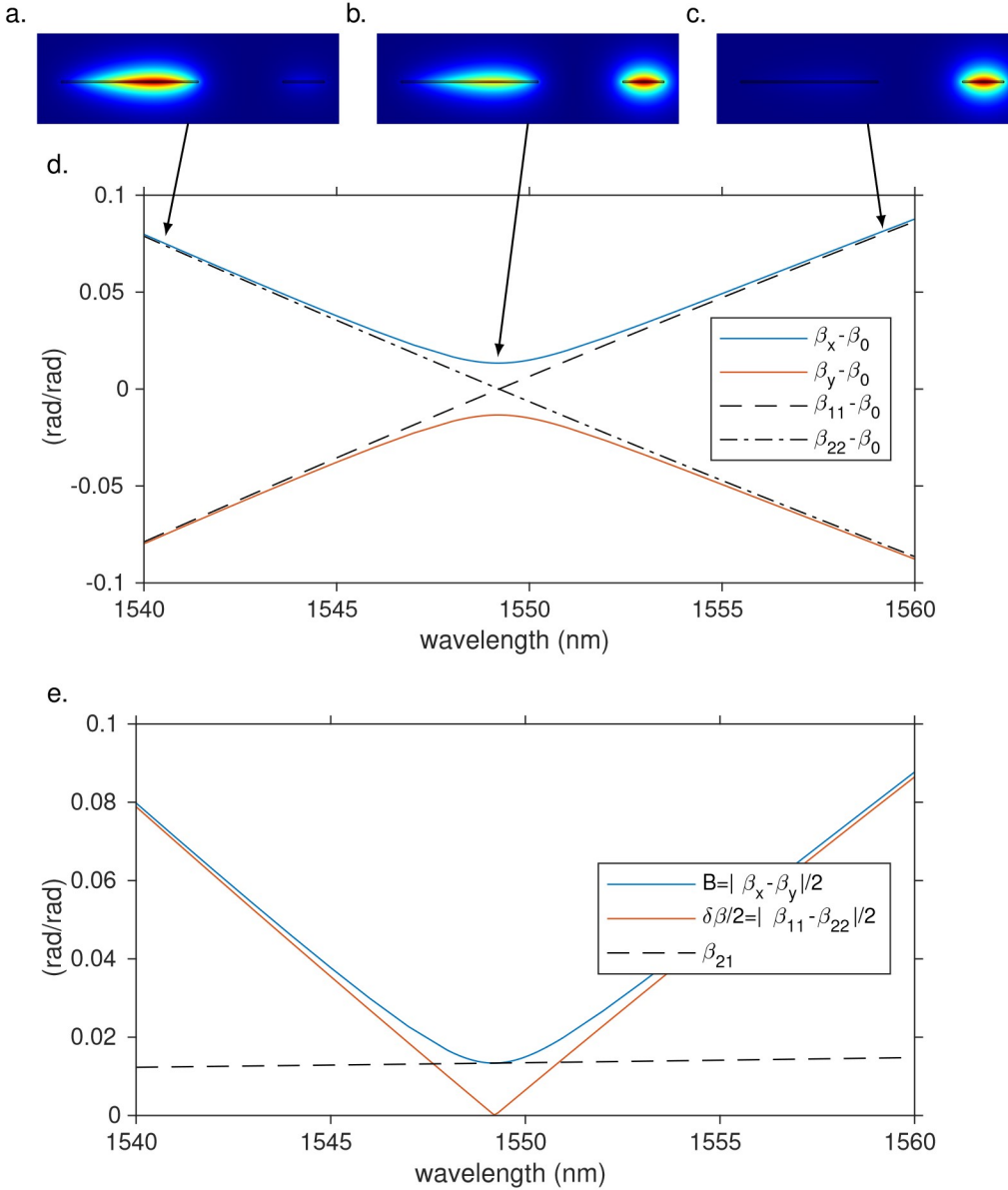


Figure 2.10: Coupling rate calculation. Eigenmodes of concentric waveguides propagating in the azimuth direction in a cylindrical geometry, with $5\text{ }\mu\text{m}$ separation, at a radius of 1 mm are shown at (a) 1540 nm, (b) 1549.2 nm, and (c) 1560 nm wavelength. (d) Propagation constants of the eigenmodes (supermodes) of the coupled waveguides, $\beta_{x,y}$, and the eigenmodes of the isolated waveguides, $\beta_{11,22}$, after subtracting the average dispersion, $\beta_0 = (\beta_{11} + \beta_{22})/2$. $\beta_{11,22}$ are matched at 1549.2 nm, leading to an avoided mode crossing for $\beta_{x,y}$. Propagation constants for the modes shown in (a), (b), and (c) are indicated. (e) B , $\delta\beta/2$, and β_{21} are calculated from the respective propagation constants shown in (d). The coupling rate β_{21} is identical to B where the propagation constants mismatch vanishes, $\delta\beta = 0$. The spectral dependence of coupling rate can be observed, which increases with increasing wavelength.

the coupling rate.

$$|\beta_{21}| = \sqrt{\left(\frac{\beta_x - \beta_y}{2}\right)^2 - \left(\frac{\delta\beta}{2}\right)^2} \quad (2.27)$$

This process is shown in Figure 2.10, for the design of a concentric directional coupler [24, 13] in 100 nm thick silicon nitride. In this simulation, the inner waveguide width was chosen as 8 μm , while outer waveguide width was chosen to match its propagation constant with the inner waveguide at approximately 1550 nm wavelength. The distance between the outer sidewall of the inner waveguide and the inner sidewall of the outer waveguide, that is, the distance between waveguides, was chosen to be 5 μm . Since the waveguides differ in geometry, they have different dispersion, and the matching condition, $\delta\beta = 0$ is precisely fulfilled only at a specific wavelength, as shown in Figure 2.10d,e. It is important to note that this situation is very different from that of a directional coupler consisting of parallel, straight waveguides; in which selecting both waveguides to have identical width guarantees the matching condition at all wavelengths due to symmetry. In Figure 2.10e, propagation constant, $\delta\beta$, the oscillation rate, B , and the coupling rate, β_{21} are calculated over the wavelength range 1540 nm to 1560 nm. The coupling rate, β_{21} , increases with increasing wavelength, due to the spectral dependence of modal confinement.

2.3.3 Selection of the coupling rate

For any desired coupling coefficient, $k = c_2(z)$, there is some freedom in the selection of the coupling rate, β_{21} . This is evident in Equation 2.22, in which, assuming that the propagation constants of the waveguides are matched, that is $B = \beta_{21}$, a choice of smaller or larger β_{21} can be compensated by a larger or smaller coupling length, z . Thus, the choice of coupling rate and coupling length merit discussion. This is particularly relevant to designs in which the directional coupler is asymmetric, as is the case in a concentric

directional coupler, because the waveguides will generally exhibit different dispersion, and the propagation constant matching condition is only fulfilled at a single wavelength for any given geometry. Furthermore, any dimensional variability in the fabrication process will likely impact the propagation constants of the respective waveguides differently, further influencing the matching of propagation constants.

From Equation 2.22, the coupling experiences a local maximum at $Bz = \pi/2$, and it is evident from Figure 2.9 that the location of this local maximum, both in coupler length, z , and in coupling amplitude, $|c_2(z)|$, is sensitive to the value of propagation constant mismatch, $\delta\beta$. Thus, if the directional coupler is designed to operate in the regime $Bz \geq \pi/2$, the coupling becomes sensitive to propagation constant mismatch, $\delta\beta$, and will be sensitive to any variability in the fabrication process.

However, it can also be seen in Figure 2.9 that in the regime $Bz < \pi/2$, the coupling amplitude is relatively invariant to propagation constant mismatch. This can be understood if we assume that $Bz \ll 1$, allowing the use of its first-order Taylor expansion to substitute $\sin(Bz) \approx Bz$ in Equation 2.22.

$$|c_2(z)|^2 = C^2 \sin^2(Bz) \approx C^2(Bz)^2 = \frac{|\beta_{21}|^2}{(\frac{1}{2}\delta\beta)^2 + |\beta_{21}|^2} \left(|\beta_{21}|^2 + \left(\frac{\delta\beta}{2}\right)^2 \right) z^2 = |\beta_{21}|^2 z^2 \quad (2.28)$$

Thus, if the requirement $Bz \ll 1$ can be met, the coupling is determined only by the coupling rate, β_{21} , and the coupler length, z ; and the propagation constant mismatch $\delta\beta$ does not impact coupling, leading to a more fabrication-tolerant design. As long as the desired coupling, k is small, that is, $k = c_2(z) \ll 1$ (which is generally the case when designing directional couplers for high Q resonators), then a requirement of $Bz \ll 1$ leads to a condition on the tolerable mismatch

$$\frac{\delta\beta}{2} \ll \frac{1}{z} = \frac{\beta_{21}}{k} \quad (2.29)$$

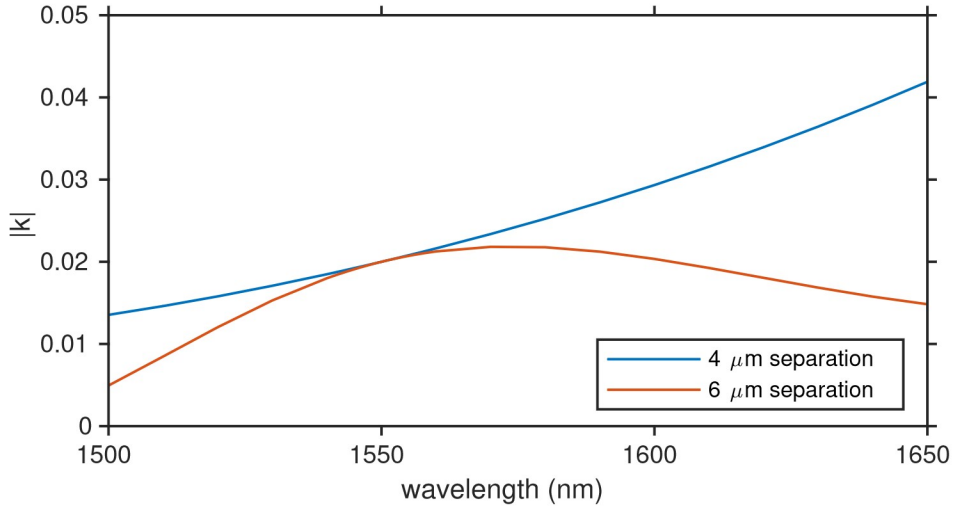


Figure 2.11: **Wavelength dependence of the coupling coefficient.** Coupling coefficient for concentric directional couplers in 100 nm thick silicon nitride at 1 mm radius, and 8 μm inner waveguide width. The couplers are both designed to be propagation-constant-matched at 1550 nm, and to have coupling coefficient of $k = 0.02$ at 1550 nm. In the coupler with smaller, 4 μm separation between waveguides, the coupling coefficient increases monotonically. In the coupler with the larger, 6 μm separation between waveguides, the coupling coefficient exhibits a local maximum.

Thus, for a fixed coupling strength, k , the choice of length of the directional coupler, z , determines the sensitivity to propagation constant mismatch. Longer coupling regions (larger z) with weaker coupling strength (smaller β_{21}) tolerate less mismatch. Shorter coupling regions (smaller z) with stronger coupling strength (larger β_{21}) can tolerate greater mismatch. This is demonstrated in Figure 2.11 for two concentric directional couplers at a radius of 1 mm and with 8 μm inner waveguide width, similar to the directional coupler designed for Figure 2.10. In Figure 2.11, both couplers are designed to be matched at 1550 nm, while their lengths are chosen to achieve a coupling coefficient of $k = 0.02$ at 1550 nm as well. The coupler with 4 μm separation between waveguides (the distance between the outer sidewall of the inner waveguide, and the inner sidewall of the outer waveguide) requires 0.44 rad coupling length to reach the desired coupling, whereas the coupler with 6 μm separation requires 4.8 rad of coupling length. The coupling coefficient, k , of the 4 μm separation directional coupler increases with wavelength because

the coupling rate, β_{21} , increases with wavelength, similar to the the coupler with 5 μm separation in Figure 2.10e. However, the coupling rate is much smaller, and the length much longer, at 6 μm separation. As a result, $|k|$ exhibits a local maximum as increasing coupling rate towards longer wavelength is outweighed by increasing propagation constant mismatch away from the 1550 nm wavelength at which the propagation constants are matched. In applications where the dependence of coupling coefficient on wavelength should be flat, the coupler can be designed to intentionally introduce propagation constant mismatch at the operating wavelength.

While a long coupling region, with a low coupling rate, would seem detrimental due to increased sensitivity to propagation constant mismatch from fabrication tolerances, it does convey benefit in the form of more selective coupling. In a concentric directional coupler, the inner waveguide is generally wider, and may support multiple transverse modes, while the outer waveguide may only support a single mode. If the directional coupler is designed such that the propagation constant of the outer waveguide is matched to the fundamental mode of the inner waveguide, then the parasitic coupling of the outer waveguide to the higher-order modes of the inner waveguide may also be calculated using Equation 2.22. While the propagation constant mismatch to the higher order modes of the inner waveguide ($\delta\beta$) are determined by the geometry of the inner waveguide, reducing the coupling rate of the outer waveguide to the fundamental mode of the inner waveguide also reduces the interaction of the outer waveguide with the higher-order modes of the inner waveguide (β_{21}), which reduces the maximum amount of power that may be transferred to undesired modes via Equation 2.23. Thus, it is possible to design a directional coupler to couple selectively to a particular mode of a waveguide which supports multiple transverse modes by reducing the coupling rate while increasing the coupling length.

2.3.4 Effective coupling length

The calculation and selection of the coupling rate, β_{21} has been addressed. However, for a parallel, straight waveguide directional coupler, as well as for a concentric, curved waveguide directional coupler, accurately determining the coupling length is necessary to calculate the overall coupling coefficient, k , of the directional coupler *a priori*. For a parallel directional coupler, the coupling rate is expressed in units of rad m^{-1} , and the coupling length is expressed in meters. For the concentric directional coupler, the coupling rate is expressed in units of rad rad^{-1} , and the coupling length is an arc length, in radians. In both cases however, calculating the coupling based on the length over which the directional coupler maintains an invariant cross-section, and the coupling rate within this region, will underestimate the coupling coefficient .

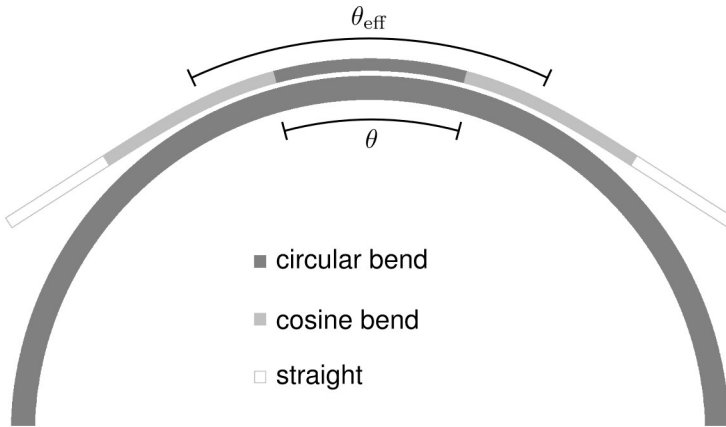


Figure 2.12: **Schematic of a concentric directional coupler.** The lower (inner) waveguide follows a perfectly circular bend, with constant curvature. The upper (outer) waveguide is concentric with the lower (inner) waveguide within the coupling region, over an arc length designated as θ . Adiabatic transitions derived from a cosine curve are used to approach the coupling region gradually, such that the effective coupling arc length spans both the circular bend and parts of the cosine bends, designated as θ_{eff} .

In Figure 2.12, the directional coupler cross-section remains invariant over an arc length, θ . In the pictured schematic, cosine bends are used to adiabatically transition from a straight routing waveguide to a curved waveguide in the vicinity of the directional

coupler. These adiabatic transitions also contribute to the coupling. From a theoretical perspective, Equation 2.15 could accommodate gradual (adiabatic) spatial variation in the coupling matrix β_{nm} , and the coupling could be integrated over the full length to include the impact of the adiabatic transitions to the coupling region. In practice, it is sufficient to empirically estimate an effective coupling arc length, $z = \theta_{\text{eff}}$ that is larger than θ , which, combined with the calculated coupling rate, β_{21} , can be used to calculate the coupling coefficient, k , using Equation 2.22.

The empirical method used in this work was to determine a threshold separation at which the coupling rate, β_{21} , is decreased by a factor of $\sqrt{2}$ from the designed value. For example, in the coupler designed in Figure 2.10, the coupling rate at separation of 5.25 μm is smaller than the coupling rate at 5 μm separation by approximately this factor, and the effective coupler length can be estimated as the arc length of the coupler for which the separation of the two waveguides does not exceed 5.25 μm . The choice of the reduction factor does not need to be precise, as the separation between waveguides within the adiabatic transition increases quadratically with distance beyond the coupling region. Thus, whether the reduction factor is chosen as $\sqrt{2}$ or 2, both result in approximately the same effective coupling length, and the deviation of the fabricated couplers from the desired coupling coefficient designed by this method which was generally observed to be below the variability in the coupling coefficient due to fabrication tolerances.

By this method, it is also possible to model a directional coupler formed between a straight waveguide and a curved waveguide. This is a common configuration for coupling to a perfectly circular ring resonator, as it is a simple structure to specify and draw. In this case the linear propagation constant of the straight waveguide can be approximately converted to the cylindrical coordinate system of the curved waveguide by multiplying by its distance from the center of curvature. The coupling rate may be approximated for the waveguide separation where the straight waveguide reaches minimum separation with

the curved waveguide. The effective coupling length may be estimated by the method described above. In this case, the straight waveguide to curved waveguide directional coupler can be considered a special case of a short, concentric directional coupler. From the prior discussion on the selection of coupling rate, a few properties of the straight-to-curved coupler can be inferred. Due to short coupling length, straight-to-curved couplers will require narrower space between the coupled waveguides to achieve a high coupling rate. If a particularly high coupling coefficient ($k \approx 1$) is required, then this may lead to excess loss in the directional coupler, as it becomes less adiabatic. In turn, if either straight or curved waveguide is multimode, the large coupling rate reduces the selectivity of the propagation-constant-matching condition. This makes the coupler more susceptible to coupling to undesired modes.

2.3.5 Sine bend adiabatic transition

In order to connect between straight waveguides and curved waveguides, a transition was developed based on sine bends with an adiabatic transition of the curvature. Such transitions were used throughout this work in order to draw racetrack resonators, as well as to transition the the curvature of the bus waveguide for concentric directional couplers. The adiabatic sine bends used in this work were defined by the following parametric curve,

$$t = [0, 1] \quad (2.30)$$

$$x(t) = \frac{\pi}{2} t R \sqrt{c} \quad (2.31)$$

$$y(t) = c R \sin \frac{\pi}{2} t \quad (2.32)$$

in which t is the parametric variable, and $x(t)$ and $y(t)$ are the parametric functions determining the coordinates of the bend. At $t = 1$, the curvature of the bend is $-1/R$, such that it may be connected to a circular bend of radius R . At $t = 0$, the curvature is zero, such that it may be connected to a straight waveguide. The parameter c allows the adiabaticity of the bend to be adjusted, such that larger values of c correspond to longer adiabatic transitions, while smaller values of c correspond to shorter adiabatic transitions. The value of c was generally chosen such that $c < 1$.

Summary

Proper design is a key ingredient for successfully achieving low-loss photonic integrated circuits. This chapter has presented the design considerations underpinning the choice of waveguide geometry, to minimize propagation loss caused by the waveguide sidewall, to ensure a single mode waveguide, as well as to ensure that losses dependent on the waveguide geometry, such as bending loss and substrate leakage, were negligible. At the device level, the resonator, a key building-block device, was introduced, and two models for its operation were presented. Finally, a coupled mode theory was applied to model the operation of a directional coupler, applicable to designs with both Cartesian and cylindrical symmetry. Practical considerations for the design, such as selection of the coupling strength, the effective coupling length, and sine-bend transitions for adiabatic change in curvature, were also discussed. The contents of this chapter formed the basis for the design of the photonic integrated circuits presented in the following chapters.

Bibliography

- [1] C. G. Roeloffzen, L. Zhuang, C. Taddei, A. Leinse, R. G. Heideman, P. W. van Dijk, R. M. Oldenbeuving, D. A. Marpaung, M. Burla, and K.-J. Boller, *Silicon nitride microwave photonic circuits*, *Optics Express* **21** (2013), no. 19 22937–22961.
- [2] K. Wörhoff, R. G. Heideman, A. Leinse, and M. Hoekman, *TriPleX: a versatile dielectric photonic platform*, *Advanced Optical Technologies* **4** (2015), no. 2 189–207.
- [3] D. J. Blumenthal, R. Heideman, D. Geuzebroek, A. Leinse, and C. Roeloffzen, *Silicon nitride in silicon photonics*, *Proceedings of the IEEE* **106** (2018), no. 12 2209–2231.
- [4] J. Liu, G. Huang, R. N. Wang, J. He, A. S. Raja, T. Liu, N. J. Engelsen, and T. J. Kippenberg, *High-yield, wafer-scale fabrication of ultralow-loss, dispersion-engineered silicon nitride photonic circuits*, *Nature communications* **12** (2021), no. 1 1–9.
- [5] X. Ji, F. A. Barbosa, S. P. Roberts, A. Dutt, J. Cardenas, Y. Okawachi, A. Bryant, A. L. Gaeta, and M. Lipson, *Ultra-low-loss on-chip resonators with sub-milliwatt parametric oscillation threshold*, *Optica* **4** (2017), no. 6 619–624.
- [6] M. H. Pfeiffer, J. Liu, A. S. Raja, T. Morais, B. Ghadiani, and T. J. Kippenberg, *Ultra-smooth silicon nitride waveguides based on the Damascene reflow process: fabrication and loss origins*, *Optica* **5** (2018), no. 7 884–892.
- [7] J. F. Bauters, M. J. Heck, D. D. John, J. S. Barton, C. M. Bruinink, A. Leinse, R. G. Heideman, D. J. Blumenthal, and J. E. Bowers, *Planar waveguides with less*

- than 0.1 dB/m propagation loss fabricated with wafer bonding, *Optics Express* **19** (2011), no. 24 24090–24101.
- [8] J. F. Bauters, M. J. Heck, D. John, D. Dai, M.-C. Tien, J. S. Barton, A. Leinse, R. G. Heideman, D. J. Blumenthal, and J. E. Bowers, *Ultra-low-loss high-aspect-ratio Si₃N₄ waveguides*, *Optics Express* **19** (2011), no. 4 3163–3174.
- [9] T. Barwicz and H. A. Haus, *Three-dimensional analysis of scattering losses due to sidewall roughness in microphotonic waveguides*, *Journal of Lightwave Technology* **23** (2005), no. 9 2719.
- [10] T. Herr, V. Brasch, J. D. Jost, C. Y. Wang, N. M. Kondratiev, M. L. Gorodetsky, and T. J. Kippenberg, *Temporal solitons in optical microresonators*, *Nature Photonics* **8** (2014), no. 2 145–152.
- [11] A. L. Gaeta, M. Lipson, and T. J. Kippenberg, *Photonic-chip-based frequency combs*, *nature photonics* **13** (2019), no. 3 158–169.
- [12] X. Ji, J. Liu, J. He, R. N. Wang, Z. Qiu, J. Riemensberger, and T. J. Kippenberg, *Compact, spatial-mode-interaction-free, ultralow-loss, nonlinear photonic integrated circuits*, *arXiv preprint arXiv:2109.06764* (2021).
- [13] W. Jin, Q.-F. Yang, L. Chang, B. Shen, H. Wang, M. A. Leal, L. Wu, M. Gao, A. Feshali, M. Paniccia, *et. al.*, *Hertz-linewidth semiconductor lasers using CMOS-ready ultra-high-Q microresonators*, *Nature Photonics* **15** (2021), no. 5 346–353.
- [14] J. F. Bauters, M. Heck, D. Dai, J. Barton, D. Blumenthal, and J. Bowers, *Ultralow-loss planar Si₃N₄ waveguide polarizers*, *IEEE Photonics Journal* **5** (2012), no. 1 6600207–6600207.

- [15] K. J. Vahala, *Optical microcavities*, *Nature* **424** (2003), no. 6950 839–846.
- [16] A. Yariv, *Universal relations for coupling of optical power between microresonators and dielectric waveguides*, *Electronics letters* **36** (2000), no. 4 321–322.
- [17] A. Yariv, *Critical coupling and its control in optical waveguide-ring resonator systems*, *IEEE Photonics Technology Letters* **14** (2002), no. 4 483–485.
- [18] D. G. Rabus, *Integrated ring resonators*. Springer, 2007.
- [19] L. A. Coldren, S. W. Corzine, and M. L. Mashanovitch, *Diode lasers and photonic integrated circuits*, vol. 218. John Wiley & Sons, 2012.
- [20] M. L. Gorodetsky, A. D. Pryamikov, and V. S. Ilchenko, *Rayleigh scattering in high-Q microspheres*, *JOSA B* **17** (2000), no. 6 1051–1057.
- [21] F. Morichetti, A. Canciamilla, and A. Melloni, *Statistics of backscattering in optical waveguides*, *Optics letters* **35** (2010), no. 11 1777–1779.
- [22] H. Kroemer, *Quantum mechanics: For engineering, materials science, and applied physics*. Pearson, 1994.
- [23] R. v. Schmidt and R. Alferness, *Directional coupler switches, modulators, and filters using alternating $\delta\beta$ techniques*, *IEEE Transactions on Circuits and Systems* **26** (1979), no. 12 1099–1108.
- [24] D. T. Spencer, J. F. Bauters, M. J. Heck, and J. E. Bowers, *Integrated waveguide coupled Si_3N_4 resonators in the ultrahigh-Q regime*, *Optica* **1** (2014), no. 3 153–157.